Biogeosciences

Discussions

EGU

1 **Physical mechanisms for biological carbon uptake during the onset of the spring**

2 **phytoplankton bloom in the northwestern Mediterranean Sea (BOUSSOLE site)**

3 Liliane Merlivat[1], Michael Hemming [2], Jacqueline Boutin[1], David Antoine[3, 4], Vincenzo

4 Vellucci[5], Melek Golbol[5], Gareth A. Lee[6], Laurence Beaumont[7]

5 [1] Sorbonne Université, CNRS/IRD/MNHN, LOCEAN, IPSL, Paris, France

6 [2] Coastal and Regional Oceanography Lab, School of Mathematics and Statistics, University

7 of New South Wales, Sydney, New South Wales, Australia

8 [3] Remote Sensing and Satellite Research Group, School of Earth and Planetary Sciences,

9 Curtin University, Perth, WA 6845, Australia

10 [4] Sorbonne Université, CNRS, Laboratoire d'Océanographie de Villefranche, Villefranche sur

11 Mer 06230, France

12 [5] Sorbonne Université, CNRS, Institut de la Mer de Villefranche, Villefranche sur Mer 06230,

13 France

14 [6] Centre for Ocean and Atmospheric Sciences, School of Environmental Sciences, University

15 of East Anglia, Norwich Research Park, Norwich NR4 7TJ, UK

16 [7] Division Technique INSU-CNRS, 92195 Meudon CEDEX, France

17

18 Correspondence to: liliane.merlivat@gmail.com

19 Keywords : Bloom onset ; Carbon uptake ; Air-sea interaction; Mediterranean sea

20 Abstract

21 Several trigger mechanisms have been proposed for the onset of the phytoplankton spring

22 bloom. Among these, that phytoplankton cells begin to bloom when they experience higher

23 average light levels in shallower mixed layers, a result of the surface net heat fluxes becoming

24 positive and wind strength decreasing. We study the impact of these two forcings in the

25 northwestern Mediterranean Sea. We take advantage of hourly measurements of oceanic and

26 atmospheric parameters collected at two neighboring moorings during the months of March

27 and April in the years 2016 to 2019, combined with glider data in 2016. The onset of

28   phytoplankton growth is concomitant with the start of significant biological activity detected

29   by a sudden decrease in dissolved inorganic concentrations derived from measurements in the

30   upper 10 m of the water column. A rapid reduction in wind stress following high-wind events

31   is observed at the same time. A resulting shallow mixing layer favors carbon uptake by

32   phytoplankton lasting a few days. Simultaneously, the air-sea net heat flux switches from

33   negative to positive because of changes in the latent air-sea heat flux, which is proportional to

34   the wind speed. This results in an increased thermal stratification of the ocean's surface layers.

35   In 2016, glider data show that the mixing layer is significantly shallower than the mixed layer

36   at the onset of the phytoplankton bloom. We conclude that decreases in the mixing and mixed

37   layer depths lead to the onset of the phytoplankton bloom due to the relaxation of wind speed

38   following storms. We estimate net daily community production in the mixing layer over

39   periods of 3 days between 2016 and 2019 as between 38 mmol C m^{-2} and 191 mmol C m^{-2}.

40   These results have important implications on the oceanic carbon cycle and biological

41   productivity estimates in the Mediterranean Sea in a scenario of climate-driven changes of the

42   wind regimes.

43

44

45   Introduction

46   Investigating the biological and physical mechanisms contributing to changes in air-sea CO_2

47   fluxes and affecting carbon export from the surface to the interior ocean is essential to

48   quantitatively estimate the effects of future environmental change. The magnitude of the

49   ocean sink for atmospheric CO_2 can be assessed through direct estimates of air-sea net CO_2

50   fluxes. It depends on the gradient of CO_2 partial pressure, pCO_2, between the atmosphere and

51   the surface ocean [Merlivat et al., 2015]. pCO_2 in the ocean mixed surface layer depends on

52   the relative contribution of dynamic transport, thermodynamics and biogeochemistry. The

53   biological carbon pump lowers pCO_2 and Dissolved Inorganic Carbon (DIC) at the sea

54   surface, hence a decrease in surface DIC, after the impact of physical processes have been

55   eliminated, essentially indicates the beginning of the phytoplankton spring growth. Various

56   conceptual frameworks have been proposed to explain the onset of spring blooms [Behrenfeld,

57   2010; Sverdrup, 1953]. The timing of phytoplankton spring bloom initiation depends in

58   particular on the atmospheric forcing, through wind stress and heat fluxes [Chiswell, 2011;

59   Taylor and Ferrari, 2011; Brody and Lozier, 2015; Enriquez and Taylor, 2015, Rumyantseva

60 et al, 2019]. Thus, to better understand which fundamental physical processes control the

61 timing of the onset of the bloom, in situ measurements are needed at the appropriate hourly to

62 daily timescale. It is important to draw attention to the atmospheric forcing timescale. In

63 biogeochemical ocean modeling studies, typically built on atmospheric models, reanalysis or

64 satellite data, time resolution of at best a few days are required [Mahadevan et al, 2012].
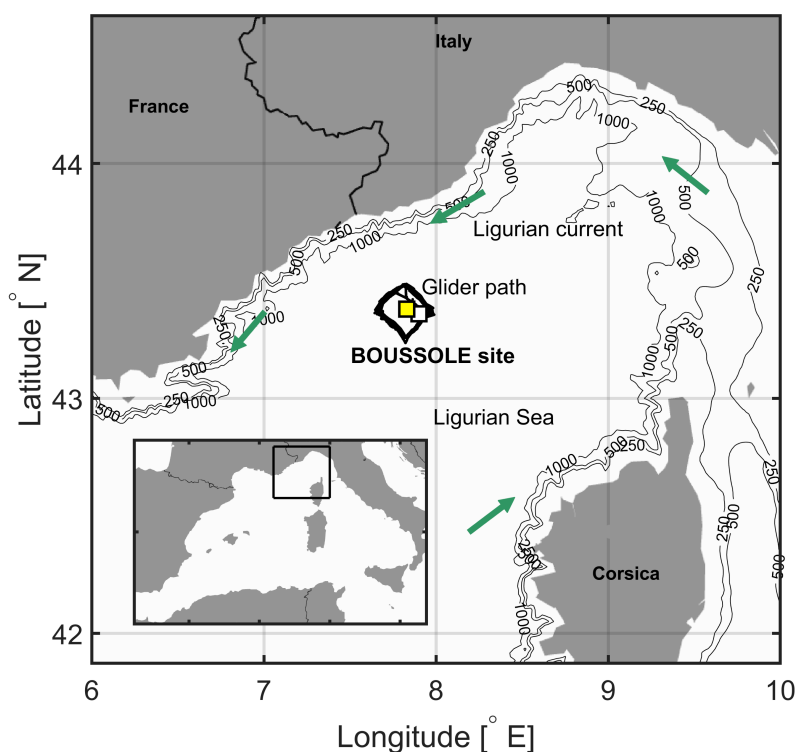
65

Figure 1. The area of the northwestern Mediterranean Sea showing the French and Italian

Rivieras, the island of Corsica, the main current branches (green arrows) in the Ligurian Sea

and the location of the BOUSSOLE buoy (white square) and the AZUR meteorological buoy

(yellow square). The black line indicates the glider's path in March-April 2016.

70 In the northwestern Mediterranean Sea, the BOUSSOLE buoy (Bouée pour l'acquisition de

71 Séries Optiques à Long Terme; Antoine et al., 2006, 2008a,b) is located in the central area of

72 the Liguro-Provençal basin (Fig.1), where the dominant ocean currents are generally weak

73 (<20 cm s^{-1}) [Millot, 1999; Antoine et al., 2008b; Niewiadomska et al., 2008]. The main

74 processes that govern the pCO$_2$ variations at the sea surface on an annual scale, after removal

75   of the temperature effect, are vertical convective mixing and biological production [Begovic
76   and Copin-Montégut, 2002; Copin-Montégut al., 2004; Hood and Merlivat, 2001; Merlivat et
77   al., 2018]. Variability of atmospheric forcing over short timescales is greatest in winter or
78   early spring [Andersen and Prieur, 2000; Antoine et al., 2008b], generating deep convection
79   that brings nutrients to the surface layer [Marty et al., 2002; Pasqueron de Fommervault et al.,
80   2015].

81   The objective of this study is to examine the impact of atmospheric forcing on phytoplankton
82   bloom initiation in the northwestern Mediterranean Sea. To this aim we use concurrent hourly
83   data of seawater carbon chemistry measured at depths less or equal to 10 m at the
84   BOUSSOLE mooring [Merlivat et al, 2018] and atmospheric flux measurements at the Azur
85   meteorological buoy 3.1 nm (5.8 km) away from BOUSSOLE in March and April 2016 to
86   2019. Additional measurements of phytoplankton chlorophyll-a (Chla), temperature and
87   density were provided by an underwater glider deployed in March-April 2016. During this
88   time, the initiation of biological carbon uptake is revealed by the sudden decrease in DIC
89   measured at the BOUSSOLE buoy.

90   In the Material and Methods section, we provide the description of data processing,
91   theoretical framework, and calculations used to evaluate mixing regimes in the water column
92   and net community production. The results section presents measured atmospheric and
93   biogeochemical parameters observed in March-April, and NCP estimates from 2016 to 2019.
94   The Discussion section relates our results to previous findings and presents our conclusions
95   regarding the drivers of phytoplankton bloom initiation.

96

97   2 Material and methods

98   2.1- Data from the BOUSSOLE mooring

99   CARIOCA sensors [Merlivat and Brault, 1995] installed on the BOUSSOLE buoy (43°22'N,
100   7°54'E; Fig.1) monitored hourly partial pressure, pCO_2, at both 3 and 10 m alongside salinity
101   and temperature (SEABIRD Scientific SBE 37 MicroCAT CTDs). Protocols for calibration of
102   in situ measurements are described in [Merlivat et al, 2018]. CARIOCA measurements of
103   pCO_2 and temperature are combined with total alkalinity (Alk) derived from salinity [Merlivat
104   et al., 2018] to calculate DIC. The dissociation constants of Mehrbach et al., (1973) refitted by
105   Dickson and Millero (1987) are used, as recommended by Alvarez et al. (2014) for the

106 Mediterranean Sea. For the March-April months mean salinity is 38.3, corresponding with

107 mean Alk equal to 2571.4 μmol kg^{-1} [Copin et al, 2004]. The expected precision of the

108 CARIOCA pCO$_2$, and DIC is 5 μatm, and 3 μmol kg$^{-1,}$ respectively [Merlivat et al, 2018].

109 2.2- Glider observations

110 An iRobot Seaglider model 1KA (SG537) with an ogive fairing operated by the University of

111 East Anglia (UEA) [see Hemming et al., 2017] was deployed during the BOUSSOLE

112 monthly cruise (#169) [Golbol et al 2000] and recovered 1 month later with a ship of

113 opportunity. Diving to 1000 m, 147 dives were completed between March 7 and April 5 2016

114 repeatedly-sampling a square-shaped path surrounding the BOUSSOLE buoy (Fig. 1) with

115 corners pointing to cardinal directions. Out of 147 dives, a number of them contain data that

116 are within 10 km of the BOUSSOLE mooring, i.e. when it was sampling in the eastern corner

117 of the diamond path. The glider was equipped with a non-pumped SEABIRD Scientific SBE

118 9 CTD instrument package providing temperature and salinity, and a WET Labs Eco Puck

119 sensor providing relative phytoplankton Chla fluorescence, factory calibrated into Chla

120 concentration units (mg m^{-3}).

121 2.3- Azur meteorological buoy

122 The Azur meteorological buoy has been deployed since 1999 by the French weather forecast

123 Agency (Meteo-France) at 43°23'N, 7°50'E (Fig. 1). It provides hourly measurements of

124 surface wind speed extrapolated to 10 m height, U_{10} (m s^{-1}), net long wave radiation, net short-

125 wave radiation, and the sensible and latent heat fluxes. These are needed to estimate the net

126 air-sea heat budget at the sea surface (http://mistrals.sedoo.fr). U_{10} is used to calculate wind

127 stress, τ, as follows: $\tau = \rho_a \, C_d \, U_{10}^2$, where ρ_a is air density (1.2 kg m^{-3}), and C_d is the drag

128 coefficient (1.4 x 10^{-3}). Photosynthetically Active Radiation (PAR, μmol quanta m^{-2} s^{-1}) is

129 related to solar irradiance (i.e. short-wave flux), SW, following PAR = 0.473 SW

130 [Papaioannou et al., 1993].

131 2.4- Estimation of mixed and mixing layer depths

132 The mixing layer depth, Z_{mx}, is the upper part of a mixed layer of uniform density where

133 active turbulence occurs [Brainerd and Gregg 1995]. Several recent studies have highlighted

134 the significance of this layer to understand the phytoplankton phenology of phytoplankton

135 blooms [Brody and Lozier, 2015; Taylor and Ferrari, 2011]. Autonomous profiling floats

136 equipped with bio-optical sensors have also highlighted the importance of mixing rather than

137 mixed layers to characterize the onset and the development of a phytoplankton bloom. Wind-

138 driven and buoyancy-driven regimes control the characteristics and depth of active mixing

139 [Brody and Lozier, 2014, 2015, Ramuyantseva et al, 2015, Lacour et al, 2019, Pellichero et al,

140 2020]. Wind-driven mixing dominates in the presence of weak buoyancy forcing when heat

141 fluxes are small. In that case, the dominant mixing length scale is equal to the Ekman length

142 layer depth scale.

143 The daily mean mixed layer depth, Z_{ml} is derived for 2016 from glider vertical profiles of

144 temperature and salinity using the algorithm provided by Holte and Talley, (2009). To

145 estimate Z_{mx}, τ is used to calculate the Ekman layer depth, Z_{ek}, $Z_{ek} = \gamma\, u_*/f$, where γ is an

146 empirical constant (0.5), f is the Coriolis parameter (10^{-4} s^{-1}) over the BOUSSOLE area, and

147 u_* is the turbulent friction velocity, $u_* = \sqrt{\dfrac{\tau}{\rho_w}}$ (m s^{-1}), with ρ_w the density of the surface sea

148 water [Lacour et al, 2019]. When heat fluxes are large and positive, Enrikez and Taylor

149 (2015) proposed to express the mixing depth Z_{mx} in terms of the surface forcing, i.e. the

150 surface stress and a stabilizing surface buoyancy flux B_0, as follows:

151
$$\frac{1}{z_{mx}^2} = \frac{f^2}{(C_3\, u_*)^2} + \frac{f\, B_0}{(C_4\, u_*^2)^2} \qquad (1)$$

152 With $C_3 = 1$, $C_4 = 0.57$, $B_0 = Q\, \lambda\, g\, /c_p\, \rho_0$, where Q is the net surface heat flux, λ the thermal

153 expansion coefficient ($1.65\ 10^{-4}$ °C^{-1}), g the gravitational acceleration (9.81 m s^{-2}), c_p the

154 specific heat of water ($4\ 10^{-3}$ J kg^{-1} °C^{-1}) and ρ_0 the pure water density (1000 kg m^{-3}).

155 2.5-Estimation of euphotic zone depth

156 The euphotic depth, Z_{eu}, is generally derived as the depth where PAR is 1% of its surface

157 value. Z_{eu} can be estimated from Chla at the surface using the method described by Lee et al.

158 (2007) based on the equation of Morel and Berthon (1989):

159
$$Z_{eu} = 34\ (Chla)^{-0.39} \qquad (2)$$

160 For the period between 2017 and 2019, GlobColour merged Chla products were used, which

161 are based on satellite observations with a resolution of 25 km, and a binning period of 8 days

162 (http://www.oceancolour.org). For 2016, glider surface Chla was used to derive Zeu instead

163 of satellite measurements. We excluded glider Chla between 05:00 and 20:00 UTC affected

164 by quenching, and we applied a depth-constant offset to glider measurements using Chla

165 water samples available on March 7.

166   2.6 – Estimation of net community production

167   Biological Net Community Production rates, NCP (mmol m^{-2} day^{-1}), are calculated for

168   separate 3-day periods in March-April, 2016 to 2019 from DIC concentrations derived from

169   CARIOCA measurements, assuming that measurements in the top 10 m of the water column

170   are representative of an homogeneous mixing layer [Boutin and Merlivat, 2009; Merlivat et al,

171   2015; Pelicherro et al, 2020]. As current velocities are expected to be small [Millot, 1999;

172   Antoine et al., 2008; Niewiadomska et al., 2008], and the focus of this study is on the

173   atmospheric drivers of bloom initiation, the effect of horizontal advection at the BOUSSOLE

174   buoy is assumed negligible over the short time periods used to estimate NCP. In the study

175   area, vertical mixing events are identified by an increase in DIC resulting from upward

176   movement of high DIC Levantine Intermediate Water (LIW) at approximately 200 m depth

177   [Copin-Montégut and Bégovic, 2002]. In this study, decreases in DIC concentrations over

178   days to weeks have been identified. For these identified periods, biological production and

179   air-sea exchange are the dominant processes responsible for daily changes in DIC. We neglect

180   the eddy diffusion term as the DIC gradient at the base of the mixing layer is very weak, and

181   entrainment is not expected as changes in DIC are observed during periods of stratification.

182   NCP is thus estimated from temporal variation of the DIC integrated over Z_{mx} (DIC_{int}), and

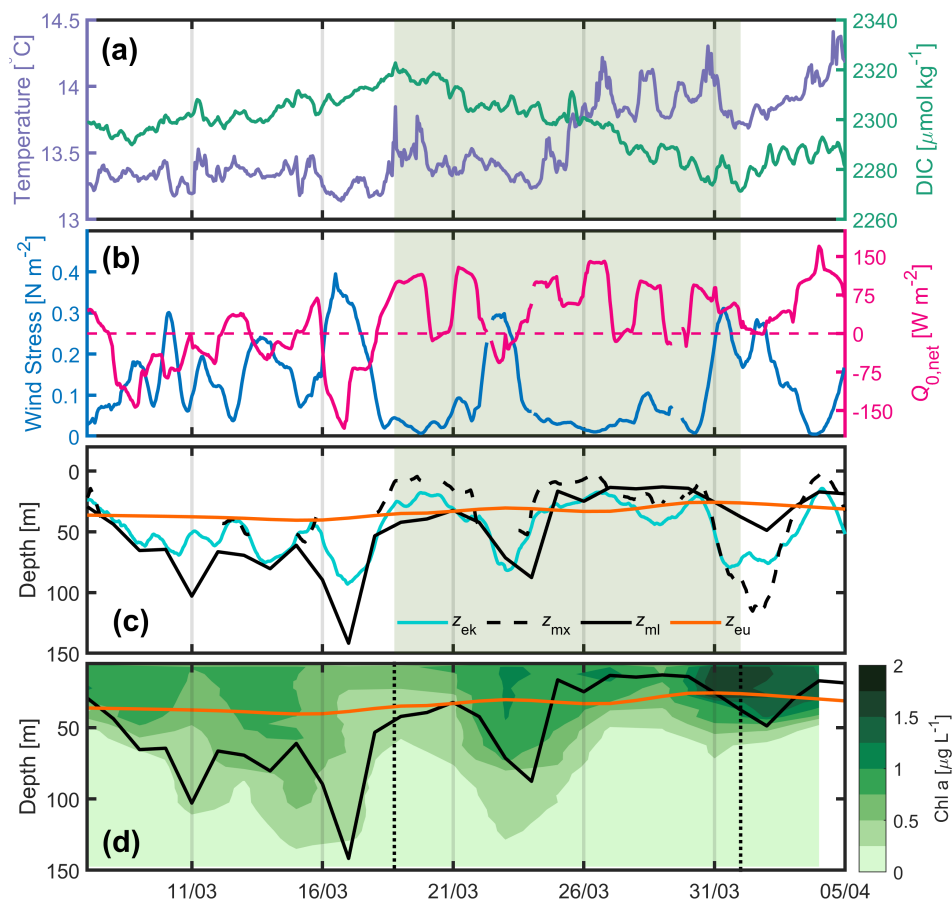183   corrected for the air-sea CO_2 flux contribution [Pelicherro et al, 2020]:

184   $$NCP = \left(\frac{\Delta DIC_{int}}{\Delta t}\right)_{bio} = \left(\frac{\Delta DIC_{int}}{\Delta t}\right)_{meas} - k \times s \times (pCO_{2atm} - pCO_{2sw}) \quad (3)$$

185   The first term in equation 3, $\left(\frac{\Delta DIC_{int}}{\Delta t}\right)_{meas}$, is the daily variation of DIC_{int} calculated over 3

186   days from the date identified as the start of phytoplankton bloom (t_0) , whilst the remaining

187   part corresponds to DIC variability due to air-sea CO_2 exchange, where k is the gas transfer

188   velocity [Wanninkhof, 2014], s is the solubility of CO_2 in seawater [Weiss, 1974], and

189   pCO_{2sw} and pCO_{2atm} are respectively the partial pressures of CO_2, in µatm, in sea water and in

190   air [Merlivat et al, 2018].

191

192   3 Results

193   3.1- Description of the 2016 time-series

194

Figure 2. 2016 (a) Hourly DIC (green) and SST(purple) at the BOUSSOLE site, (b) hourly
wind stress (blue) and net heat flux (pink) at the Azur buoy site. The pink dotted line indicates
the change of sign of the net heat flux from negative to positive values, (c) daily depths of the
mixed layer (black), mixing layer (dotted black), Ekman layer (cyan) and euphotic layer
(orange) at the BOUSSOLE site. The green background on panels (a), (b), and (c) indicates
the onset period of the bloom (18 March to 1st April). (d) Glider-derived depths of the mixed
layer (black curve, same as in (c)), euphotic layer (orange), and nighttime 2-day binned
chlorophyll concentration (green coloring) retrieved between March 7 and April 5.

The temporal evolution of physical and biogeochemical parameters between March 7 and
April 5 2016 is displayed in Fig. 2. It shows an initial increase in DIC until March 18 (Fig. 2a),

Biogeosciences
Discussions

205   resulting from the vertical mixing of surface waters with the DIC-enriched underlying LIW

206   [Copin-Montégut and Bégovic, 2002], followed by a decrease in DIC that corresponds to an

207   increase of surface Chla (Fig 2d). Temperature increases intermittently over the same time

208   period (Fig. 2a), with a sharp increase on March 18 and 25. Before March 18 frequent

209   atmospheric fronts associated with wind forcing between 0.2 and 0.5 N m^{-2} were observed

210   (Fig. 2b). $Q_{0,net}$ was negative most of the time leading up to March 18, but mostly positive

211   afterwards (Fig. 2b). A clear anticorrelation was observed between τ and $Q_{0,net}$ (Fig. 2b). The

212   mixed-layer depth derived from the glider measurements (< 20 km away from the Boussole

213   site) deepened to > 70 m at times between March 8 and March 18, consistent with the passage

214   of frequent atmospheric fronts. From March 18 to April 5, Z_{ml} shoaled from ~ 45 m to ~10 m,

215   excluding two short periods around March 24 and April 2 when atmospheric fronts were

216   passing (Fig. 2c). From March 18 to 31, Z_{mx} was for a considerable time either shallower than,

217   or at similar depth to Z_{ml} and Z_{eu} (Fig. 2c). From March 18 to April 5, an increase in glider

218   Chla was observed in the upper layer (Fig. 2d) as the result of the biomass accumulation

219   within the water column following the initial growth of phytoplankton [Behrenfeld, M. and E.

220   Boss, 2014]. The same was observed in the Southern Ocean [Pelicherro et al, 2019].

221   3.2- Description of the 2017-2018-2019 time-series

222   Only measurements at the BOUSSOLE and Azur buoys were available between 2017 and

223   2019. Here we focus on the periods between March 1 and April 25. In 2017, from March 9,

224   after the passage of a very active atmospheric front (τ up to 2.7 N m^{-2}), a decrease in DIC

225   accompanied by an increase in temperature was observed for a period of 14 days despite a

226   few short bursts of vertical mixing, typically lasting less than 1 day (Fig.3a, d, g). At the same

227   time, the net surface heat flux switched from negative to positive most of the time. Over this

228   14-day period, Z_{mx} was predominantly shallower than the Z_{eu} at times when DIC was

229   decreasing.

230   In 2018 (Fig. 3b, e, h) and 2019 (Fig. 3c, f, i), the weather records throughout the month of

231   March are very similar, showing a succession of very strong wind events at the start of the

232   investigated time periods, with τ values of up to 3.7 N m^{-2} and Z_{ek} values as deep as 300 m.

233   On April 5, 2018, following a period of high wind stress resulting in the formation of a deep

234   mixing layer (~250 m), a decrease in DIC and an increase in SST were observed over 3 days.

235   At the same time, the net heat flux oscillated around zero. In 2019, CARIOCA data were only

236   available after March 24. On March 30, 3 days after high winds, a decrease in DIC and an

237   increase in temperature lasted 3 days, while simultaneously the net heat flux reversed from

238   negative to positive.

239
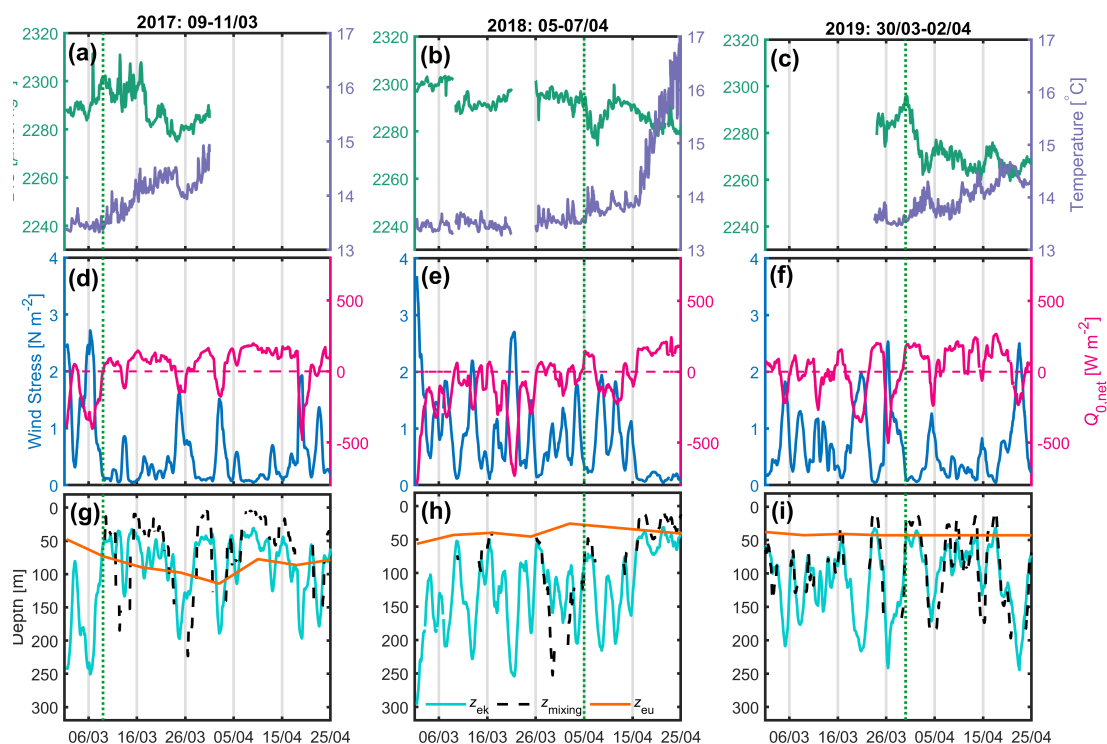
240

Figure 3. (a, b, c) 2017, 2018 and 2019 DIC (green) and SST (purple) at the BOUSSOLE site,
(d, e, f) wind stress (blue) and net heat flux (red) at the Azur buoy site. The red dotted line

indicates the change of sign of the net heat flux from negative to positive values, (g, h, i)
depths of the mixing layer (dotted black), Ekman layer (cyan) and euphotic layer (orange) at
the BOUSSOLE site. The vertical dotted green line indicates the onset of the bloom.

246   3.3- NCP

247   NCP was estimated (Eq. 3) for 3-day periods over the four time-series between 2016 and

248   2019 (Table 1). Because we compute NCP only during periods when Z_{ml} and Z_{mx} shoal and

249   the air-sea CO_2 flux is very small, the measured total daily changes of DIC, dDIC/dt

250   (correlation coefficient, $r^{*2} > 0.70$), is expected to represent the biological consumption of

251   DIC. In 2016, 2017, and 2019, daily biological carbon uptake fluxes are between 38 and 191

252   mmol m^{-2} d^{-1}. PAR varies between 63+/-3 and 113+/-2 mol photons m^{-2} d^{-1} for the four

253   considered periods (Table 2).

|	T_0	dDIC/dt [a]	r^{*2} [b]	ΔDIC / Δt [c]	r^{*2} [d]	air-sea flux CO_2 [e]	NCP [f]
		μmol $kg^{-1}d^{-1}$		mmol $m^{-2}d^{-1}$		mmol $m^{-2}d^{-1}$	mmol m^{-2} d^{-1}
2016 10m	March 18	-3.0	0.80	-37	0.68	1	38
2017 3m	March 9	-4.5	0.84	-188	0.86	3	191
2018 3m	April 5	-6.5	0.70			17	
2019 10m	March 30	-8.3	0.93	-163	0.63	4	167

254

255   Table 1. Net community production computed in the mixing layer over 3 days (NCP) after the

256   bloom onset (T_0). (a, b) variation of DIC at the measurement depth and linked correlation

257   coefficient; (c, d) change of integrated DIC over Z_{mx} and linked correlation coefficient ;(e)

258   CO_2 flux from the atmosphere to the ocean; (f), absolute value of calculated NCP is

259   considered in order to provide positive values throughout the presentation and discussion in

260   the manuscript.

261

262   4 Discussion

263   4.1 Analysis of the physical drivers of the bloom initiation over the 4 years, 2016-2019

264   In 2016, the biological consumption of carbon indicated by the decrease in DIC from March

265   18 attests the initiation of spring phytoplankton growth (Fig. 2a). Between 2 successive days,

266   March 17 and 18, a rapid decrease in daily wind stress from 0.24 to 0.04 N m^{-2} results in a

267   change of sign of the net heat flux from -68 to +56 W m^{-2} (Fig.4a) and a shoaling Z_{mx}, which

268   is for the most part shallower than Z_{eu} (Fig.4b) after March 18.
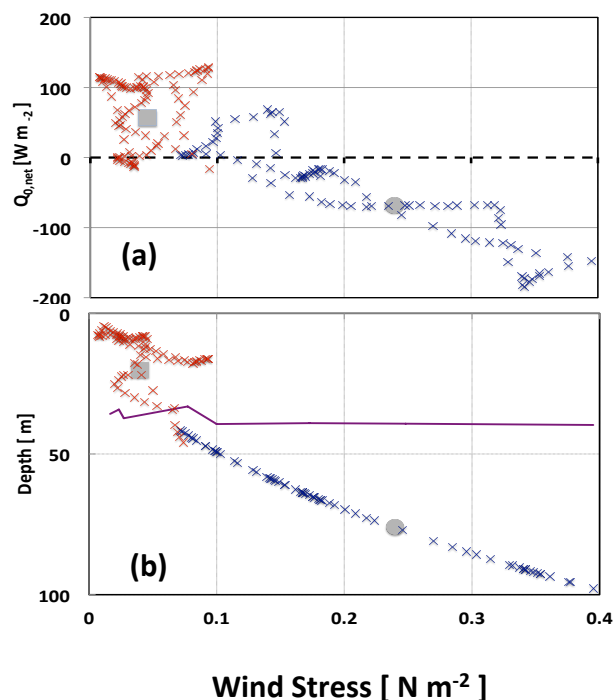
269

Figure 4. Changes of physical parameters (hourly values) at the onset of the 2016 bloom during 2 consecutive periods of 4 days, March 14-17 (blue) and March 18-21 (red) as a function of wind stress (a) net surface heat flux (b) depths of the mixing layer. Grey circles and grey squares indicate mean values respectively on March 17 and March 18. The purple line shows the euphotic layer depth (March 14-21).

This illustrates the very fast change in heat flux and mixing layer thickness resulting from the decrease in wind stress. The main drivers to explain the initiation of near surface spring phytoplankton blooms proposed by [Taylor and Ferrari, 2011, Brody-Lozier, 2014, 2015] are a decrease in wind strength, a positive surface heat flux, and a decrease in the dominant mixing length scale. Our results indicate that a decrease in τ is a common component for these last two mechanisms (Fig.4). The variability of $Q_{0,net}$ is strongly controlled by the variability of the latent heat flux proportional to the wind speed. From March 17 to 18, the latent heat flux changed by 84 W m^{-2} representing nearly 2 thirds of the total change of Q_0, with the remainder originating from an increased short-wave flux. Hence, $Q_{0,net}$ increased as τ decreased. In the same way Z_{mx}, which is related to τ and $Q_{0,net}$, decreased. This highlights the major contribution of wind stress relaxation in controlling the net surface heat flux, and

286   subsequent stratification leading to shallower Z_{mx}. Due to the seasonal increase of surface

287   irradiance in March-April, as well as the availability of nutrients following vertical mixing

288   with intermediate nutrient-enriched waters [Begovic and Copin-Montégut, 2002], the

289   conditions for the onset of the bloom are met.

290   Over the 4 years, 2016-2019, during the months of March and April, at the very beginning of

291   spring, the conditions required for initiating the spring bloom are very similar although the

292   range of wind stress values is smaller in 2016. (Fig. 2, Fig. 3). The wind stress values are low

293   following storm events. For all years except 2018, Z_{mx} is smaller than Z_{eu}. The average

294   atmospheric and oceanographic conditions during the onset of the bloom are shown in Table 2.

295   The decrease of wind-driven mixing is then a dominant physical mechanism, namely mixed

296   layer shoaling which best predicts the timing of the spring bloom [Brody Lozier, 2014, 2015].

297   Likewise, in the Southern Ocean, Pelicherro et al (2020) showed that a bloom is initiated only

298   when the wind-driven mixed layer decreases, even if the net heat flux has been positive for

299   some months.

300   4.2- Biological carbon uptake

301   In 2016, 2017, and 2019, at the onset of the bloom Z_{mx} is shallower than Z_{eu} (Table 2). Two

302   factors account for the observed large range of NCP variability at the time of triggering the

303   bloom: dDIC/dt and Z_{ml}. In 2016 and 2017, DIC decreased over a period of 14 days, whereas

304   it lasted for 3 days in 2018 and 2019, as a result of short-lived high wind events ($\tau > 1$ N m^{-2}).

305   On April 2, 2018, a high surface phytoplankton Chla, 1.9 mg m^{-3}, was measured by satellite

306   (Globcolour data) suggesting a strong biological signal. However, as Z_{eu} is significantly

307   shallower than Z_{mx} (26 m vs. 65m; Fig. 3h), it would be incorrect to estimate NCP integrated

308   over Z_{mx} using the DIC gradient measured at 3 m depth.

309   At the nearby DyFAMed site (Dynamique des Flux Atmospheriques en Mediterranee), using

310   a 20-year O_2 time series, Coppola et al. (2018) estimated an annual net community carbon

311   production equal to 7.1 mol m^{-2} yr^{-1}, or 19.4 mmol m^{-2} d^{-1}. Additionally, using

312   determinations of primary production from ^{14}C in-situ incubations and of carbon export fluxes

313   from sediment traps at DyFAMed, Marty and Chiaverini (2002) calculated average daily

314   primary productions between 19.6 and 53 mmol m^{-2} d^{-1}. These estimates may have

315   underestimated the annual NCP values as they were calculated from monthly observations

316   while phytoplankton production varies on a daily timescale. Our DIC measurements highlight

317   the large short-term variability of carbon consumption over a few days in March-April when

318 bloom-triggering atmospheric conditions are met, such as seasonal light increase and
319 availability of nutrients.

	T_0	Wind stress $_0$	Net heat flux $_0$	PAR_0	$Z_{mixing\ 0}$	$Z_{Euphotic\ 0}$
		$N\ m^{-2}$	$W\ m^{-2}$	mol photons $m^{-2}d^{-1}$	m	m
2016	March 18	0.04 +/-0.02	56+/-36	78+/-3	20+/-9	47
2017	March 9	0.12+/-0.02	45+/-21	63+/-3	28+/-12	71
2018	April 5	0.30+/-0.24	127+/-12	88+/-6	62+/-9	29
2019	March 30	0.10+/-0.02	183+/-9	113+/-2	20+/-5	43

320

321 Table 2. 2016-2019. Atmospheric drivers of the onset of the bloom: average values and
322 standard deviation on the day of the start of the bloom, T_0.

323

324 5- Concluding remarks

325 Around March and April in the northwestern Mediterranean Sea, the seasonal change in
326 lighting conditions and atmospheric forcing are the essential parameters that control the
327 triggering of near-surface phytoplankton blooms. These mechanisms have been highlighted
328 through the coupling of high-frequency physical and biogeochemical in situ observations. For
329 years 2016 to 2019, a bloom started in March or early April, following a period of intense
330 mixing. The rapid decrease in surface wind speed entailed a switch from negative to positive
331 air-sea net heat fluxes, essentially due to changes in the latent air-sea heat flux proportional to
332 wind speed. These analysis support the hypothesis that decreases in the depth of active mixing,
333 a result of the transition from buoyancy-driven to wind-driven mixing, control the timing of
334 the spring bloom.

335

336 Data availability

Biogeosciences
Discussions

Open Access

EGU

337   BOUSSOLE data (2016-2019) are available in the SEANOE data base (Merlivat Liliane,

338   Boutin Jacqueline (2020). Mediterranean Sea surface CO_2 partial pressure and temperature

339   data. SEANOE. https://doi.org/10.17882/56709

340   Meteorological buoy Azur: http://mistrals.sedoo.fr

341   SChl, 8-day, 4 kmx4 km resolution, level 3 mapped ocean colour product distributed by the

342   European Space Agency, available at http://www.ocean colour/org

343   All glider data will be archived at the British Oceanographic Data Centre

344   (BODC, https://www.bodc.ac.uk/data/bodc_database/gliders/) prior to article acceptance.

345   Author contributions: VV and MG were respectively in charge of the BOUSSOLE mooring

346   buoy maintenance and monthly water sampling. LB was responsible for the laboratory

347   preparation and calibration of the CARIOCA sensors. GAL led the UEA glider mission in

348   March-April 2016. DA and VV provided data and funding through the BOUSSOLE project

349   and contributed to writing and editing of the manuscript.

361

362   References

363   Álvarez, M., Sanleón-Bartolomé, H., Tanhua, T., Mintrop, L.,Luchetta, A., Cantoni, C.,

364   Schroeder, K., and Civitarese, G.: The CO2 system in the Mediterranean Sea: a basin wide

365   perspective, Ocean Sci., 10, 69–92, https://doi.org/10.5194/os-10-69-2014,2014.

366 Andersen, V. and Prieur, L.: One-month study in the open NW Mediterranean Sea
367 (DYNAPROC experiment, May 1995): Overview of hydrobiogeochemical structures and
368 effects of wind events, Deep-Sea Res. I, 47, 397–422, 2000.

369 Antoine, D. M. Chami, H. Claustre, F. D'Ortenzio, A. Morel, G. Bécu, B. Gentili, F. Louis ,J.
370 Ras, E. Roussier, A.J. Scott, D. Tailliez, S. B. Hooker, P. Guevel, J.-F. Desté, C. Dempsey
371 and D. Adams. 2006, BOUSSOLE : a joint CNRS-INSU, ESA, CNES and NASA Ocean
372 Color Calibration and Validation Activity. NASA Technical memorandum, N° TM-2006-
373 214147, NASA/GSFC, Greenbelt, USA.

374 Antoine, D., P. Guevel, J.-F. Desté, G. Bécu, F. Louis, A.J. Scott and P. Bardey: The
375 «BOUSSOLE» buoy; a new transparent-to-swell taut mooring dedicated to marine optics:
376 design, tests and performance at sea, Journal of Atmospheric and Oceanic Technology, 25,
377 968-989, 2008a.

378 Antoine, D., F. d'Ortenzio, S. B. Hooker, G. Bécu, B. Gentili, D. Tailliez, and A. J. Scott:
379 Assessment of uncertainty in the ocean reflectance determined by three satellite ocean color
380 sensors (MERIS, SeaWiFS and MODIS-A) at an offshore site in the Mediterranean Sea
381 (BOUSSOLE project), Journal of Geophysical Research, 113(C7), 2008b.

382 Begovic , M., and C. Copin-Montegut, Processes controlling annual variations in the partial
383 pressure of fCO2 in surface waters of the central northwestern Mediterranean sea (Dyfamed
384 site), Deep-Sea Research II, 49, 2031-2047, 2002

385 Behrenfeld, M. J, Abandoning Sverdrup's critical depth hypothesis on phytoplankton blooms.
386 Ecology, 91(4), 977-989, 2010

387 Behrenfeld, M. and E. Boss, Resurrecting the ecological underpinnings of ocean plankton
388 blooms. Annual Review of Marine Science, 6, 167-194, DOI: 10.1146/annurev-marine-
389 052913-021325, 2014

390 Brainerd, K. E., and Gregg, M. C, Surface mixed and mixing layer depths. Deep Sea Research
391 I: Oceanographic Research Papers, 42:1521–1543, 1995

392 Brody, S., and Lozier,M. Changes in dominant mixing length scale as a driver of
393 phytoplankton bloom initiation in the North Atlantic, Geophysical Research Letters 41, 3197–
394 3206, 2014.

395   Brody, S. R., & Lozier, M. S. , Characterizing upper-ocean mixing and its effect on the spring

396   phytoplankton bloom with in situ data. ICES Journal of Marine Science, 72(6), 1961-1970,

397   2015.

398   Chiswell, S. M.: Annual cycles and spring blooms in phytoplankton: don't abandon Sverdrup

399   completely. Marine Ecology Progress Series, 443, 39-50, 2011.

400   Copin-Montégut, C., Begovic, M.: Distributions of carbonate properties and oxygen along the

401   water column (0– 2000 m) in the central part of the NW Mediterranean Sea (Dyfamed site).

402   Influence of winter vertical mixing on air– sea CO_2 and O_2 exchanges. Deep-Sea Res., Part 2,

403   Top. Stud. Oceanogr. 49, 2049– 2066, 2002.

404   Copin-Montégut, C., M. Bégovic, and L. Merlivat.: Variability of the partial pressure of CO_2

405   on diel to annual time scales in the Northwestern Mediterranean Sea, Mar Chem, 85(3-4),

406   169-189, 2004.

407   Coppola, L., Legendre, L., Lefevre, D., Prieur, L., Taillandier, V., & Riquier, E. D. :

408   Seasonal and inter–annual variations of dissolved oxygen in the northwestern Mediterranean

409   Sea (DYFAMED site). Progress in Oceanography, 2018.

410   Dickson, A. G., and F. J. Millero .: A comparison of the equilibrium constants for the

411   dissociation of carbonic acid in seawater media, Deep Sea Research Part A. Oceanographic

412   Research Papers, 34(10), 1733-1743 1987.

413   Enriquez, R.M., Taylor, J.R: Numerical simulations of the competition between wind-driven

414   mixing and surface heating in triggering spring phytoplankton blooms. ICES J. Mar. Sci. J. du

415   Cons. fsv071, 2015.

416   Golbol, M., Vellucci, V., Antoine, D .: BOUSSOLE, https://doi.org/10.18142/1, 2000.

417   Hemming, M. P., Kaiser, J., Heywood, K. J., Bakker, D. C., Boutin, J., Shitashima, K., Onken,

418   R. : Measuring pH variability using an experimental sensor on an underwater glider. Ocean

419   Science, 13 , 427–442,2017.

420   Holte, J., & Talley, L. : A new algorithm for finding mixed layer depths with applications to

421   Argo data and Subantarctic Mode Water formation. Journal of Atmospheric and Oceanic

422   Technology, 26(9), 1920-1939, 2009.

423   Hood, E. M., and L. Merlivat .: Annual and interannual variations of fCO2 in the
424   northwestern Mediterranean Sea: Results from hourly measurements made by CARIOCA
425   buoys, 1995-1997, J Mar Res, 59, 113-131, 2001.

426   Lacour, L., Briggs, N., Claustre, H., Ardyna, M., & Dall'Olmo, G.: The intraseasonal
427   dynamics of the mixed layer pump in the subpolar North Atlantic Ocean: A Biogeochemical-
428   Argo float approach. Global Biogeochemical Cycles, 33(3), 266–281,2019.

429   Lee, Z., Weidemann, A., Kindle, J., Arnone, R., Carder, K. L., & Davis, C. : Euphotic

430   zone depth: Its derivation and implication to ocean-color remote sensing. Journal of
431   Geophysical Research: Oceans , 112 (C3),2007.

432   Mahadevan, A., D'asaro, E., Lee, C., & Perry, M. J. : Eddy-driven stratification initiates
433   North Atlantic spring phytoplankton blooms. Science, 337(6090), 54-58, 2012.

434   Marty, J.-C, Chiavérini, J. .: Seasonal and interannual variations in phytoplankton

435   production at DYFAMED time-series station, northwestern Mediterranean Sea. Deep

436   Sea Res. Part II 49, 2017–2030, 2002.

437   Mehrbach, C., C. H. Culberson, J. E. Hawley, and R. M. Pytkowicx .: Measurement of the
438   apparent dissociation constants of carbonic acid in seawater at atmospheric pressure, Limnol
439   Oceanogr, 18(6), 897-907, 1973.

440   Merlivat, L., and Brault, P.: CARIOCA BUOY, Carbon Dioxide Monitor, Sea Technol., 23–
441   30, 1995.

442   Merlivat, L., Boutin, J., & Antoine, D. : Roles of biological and physical processes in driving
443   seasonal air–sea CO 2 flux in the Southern Ocean: New insights from CARIOCA pCO 2.
444   Journal of Marine Systems, 147, 9-20, 2015.

445   Merlivat, L., Boutin, J., Antoine, D., Beaumont, L., Golbol, M., & Vellucci, V. : Increase of
446   dissolved inorganic carbon and decrease of pH in near surface waters of the Mediterranean
447   Sea during the past two decades. Biogeosciences, 15(18), 5653-5662, 2018.

448   Millot: Circulation in the Western Mediterranean Sea, Journal of Marine Systems, 20, 423–
449   442, 1999.

450 Morel, A., and J. F. Berthon . : Surface pigments, algal biomass profiles, and potential

451 production of the euphotic layer: relationships reinvestigated in review of remote-sensing

452 applications, Limnol. Oceanogr., 34, 1545–1562, 1989.

453 Niewiadomska, Katarzyna, Claustre, Hervé, Prieur, Louis, d'Ortenzio, Fabrizio, (2008),

454 Submesoscale physical-biogeochemical coupling across the Ligurian current (northwestern

455 Mediterranean) using a bio-optical glider, Limnology and Oceanography, 53, doi:

456 10.4319/lo.2008.53.5_part_2.2210.

457 Papaioannou, G., Papanikolaou, N., and Retalis, D. : Relationships of photosynthetically

458 active radiation and shortwave irradiance. Theoretical and Applied Climatology, 48: 23–27,

459 1993.

460 Pasqueron de Fommervault, O., Migon, C., D'Ortenzio, F., Ribera d'Alcalà, M., and Coppola,

461 L.: Temporal variability of nutrient concentrations in the northwestern Mediterranean sea

462 (DYFAMED time-series station), Deep-Sea Res. Pt. I, 100, 1–12, 2015.

463 Pellichero, V., Boutin, J., Claustre, H., Merlivat, L., Sallée, J.-B., & Blain, S. : Relaxation of

464 wind stress drives the abrupt onset of biological carbon uptake in the Kerguelen bloom: a

465 multisensory   approach.   Geophysical   Research

466 Letters,47,https://doi.org/10.1029/2019GL085992 , 2020.

467 Sverdrup, H. U.: On vernal blooming of phytoplankton. Conseil Exp. Mer, 18, 287-295,1953.

468 Rumyantseva, A, Henson, S, Martin,A , Thompson, A. F, Damerell G.M, Kaiser J, Heywood,

469 K.J.: Phytoplankton spring bloom initiation: The impact of atmospheric forcing and light in

470 the temperate North Atlantic Ocean, Progress in Oceanography, 2019.

471 Taylor, J. R., & Ferrari, R.: Shutdown of turbulent convection as a new criterion for the onset

472 of spring phytoplankton blooms. Limnology and Oceanography, 56(6), 2293-2307, 2011.

473 Wanninkhof, R.: Relationship between wind speed and gas exchange over the ocean revisited.

474 Limnology and Oceanography: Methods, 12(6), 351–362, 2014.

475 Weiss, R.: Carbon dioxide in water and seawater: the solubility of a non-ideal gas, Marine

476 chemistry , 2 (3), 203–215, 1974

477

478

479   Figures and tables

480   Figure 1. The area of the northwestern Mediterranean Sea showing the French and Italian
481   Rivieras, the island of Corsica, the main current branches (green arrows) in the Ligurian Sea
482   and the location of the BOUSSOLE buoy (white square) and the AZUR meteorological buoy
483   (yellow square). The black line indicates the glider's path in March-April 2016.

484   Figure 2. 2016 (a) Hourly DIC (green) and SST(purple) at the BOUSSOLE site, (b) hourly
485   wind stress (blue) and net heat flux (pink) at the Azur buoy site. The pink dotted line indicates
486   the change of sign of the net heat flux from negative to positive values, (c) daily depths of the
487   mixed layer (black), mixing layer (dotted black), Ekman layer (cyan) and euphotic layer
488   (orange) at the BOUSSOLE site. The green background on panels (a), (b), and (c) indicates
489   the onset period of the bloom (18 March to 1st April). (d) Glider-derived depths of the mixed
490   layer (black curve, same as in (c)), euphotic layer (orange), and nighttime 2-day binned
491   chlorophyll concentration (green coloring) retrieved between March 7 and April 5.

492   Figure 3. (a, b, c) 2017, 2018 and 2019 DIC (green) and SST (purple) at the BOUSSOLE site,
493   (d, e, f) wind stress (blue) and net heat flux (red) at the Azur buoy site. The red dotted line
494   indicates the change of sign of the net heat flux from negative to positive values, (g, h, i)
495   depths of the mixing layer (dotted black), Ekman layer (cyan) and euphotic layer (orange) at
496   the BOUSSOLE site. The vertical dotted green line indicates the onset of the bloom.

497   Figure 4. Changes of physical parameters (hourly values) at the onset of the 2016 bloom
498   during 2 consecutive periods of 4 days, March 14-17 (blue) and March 18-21 (red) as a
499   function of wind stress (a) net surface heat flux (b) depths of the mixing layer. Grey circles
500   and grey squares indicate mean values respectively on March 17 and March 18. The purple
501   line shows the euphotic layer depth (March 14-21).

502   Table 1. Net community production computed in the mixing layer over 3 days (NCP) after the
503   bloom onset (T_0). (a, b) variation of DIC at the measurement depth and linked correlation
504   coefficient; (c, d) change of integrated DIC over Z_{mx} and linked correlation coefficient ;(e)
505   CO_2 flux from the atmosphere to the ocean; (f), absolute value of calculated NCP is
506   considered in order to provide positive values throughout the presentation and discussion in
507   the manuscript.

508   Table 2.   2016-2019. Atmospheric drivers of the onset of the bloom: average values and

509   standard deviation on the day of the start of the bloom, T_0.

510